Double and Quadruple Flat Bands Tuned by Alternative Magnetic Fluxes in Twisted Bilayer Graphene

Congcong Le,[1] Qiang Zhang,[2] Fan Cui,[2,3] Xianxin Wu,[4,*] and Ching-Kai Chiu[1,†]
[1]RIKEN Interdisciplinary Theoretical and Mathematical Sciences (iTHEMS), Wako, Saitama 351-0198, Japan
[2]Institute of Physics, Chinese Academy of Sciences, Beijing 100190, China
[3]University of Chinese Academy of Sciences, Beijing 100049, China
[4]CAS Key Laboratory of Theoretical Physics, Institute of Theoretical Physics, Chinese Academy of Sciences, Beijing 100190, China

(Received 17 November 2022; revised 27 November 2023; accepted 6 May 2024; published 13 June 2024)

Twisted bilayer graphene (TBG) can host the moiré energy flat bands with twofold degeneracy serving as a fruitful playground for strong correlations and topological phases. However, the number of degeneracy is not limited to two. Introducing a spatially alternative magnetic field, we report that the induced magnetic phase becomes an additional controllable parameter and leads to an undiscovered generation of fourfold degenerate flat bands. This emergence stems from the band inversion at the Γ point near the Fermi level with a variation of both twisted angle and magnetic phase. We present the conditions for the emergence of multifold degenerate flat bands, which are associated with the eigenvalue degeneracy of a Birman-Schwinger operator. Using holomorphic functions, which explain the origin of the double flat bands in the conventional TBG, we can generate analytical wave functions in the magnetic TBG to show absolute flatness with fourfold degeneracy. Moreover, we identify an orbital-related intervalley coherent state as the many-body ground state at charge neutrality. In contrast, the conventional TBG has only two moiré energy flat bands, and the highly degenerate flat bands with additional orbital channels in this magnetic platform might bring richer correlation physics.

DOI: 10.1103/PhysRevLett.132.246401

Introduction.—Moiré twistronics, focusing on the exotic properties of moiré superlattcies from two-dimensional (2D) twisted van der Waals multilayers, has attracted enormous attention in contemporary research [1–10]. One well-known example is the twisted bilayer graphene (TBG), where moiré interlayer coupling can significantly alter the low-energy physics, and its electronic structure is described by the Bistrizer-MacDonald model for a small twisted angle [1]. Most prominently, when the twisted angle is adjusted to be magic values, the low-energy Dirac bands evolve to isolated twofold flat bands (FBs) with "fragile" topology [4]. Thus, these FBs in the TBG offer an exciting playground to explore emergent correlated and topological physics, and a wide range of intriguing correlated phenomena have been experimentally observed, such as correlated insulating states [2,5,11–15], unconventional superconductivity [3,5,15–18], and the quantum anomalous Hall effect [19–22].

When chiral symmetry is preserved, at magic angles the moiré FBs are absolutely flat in the entire moiré Brillouin zone (BZ). This absolute flatness can be proved by the construction of the wave functions (WFs) from holomorphic functions [23]. In addition, calculating the spectral of a compact Birman-Schwinger operator can precisely determine all real magic angles for the twofold FBs (per valley/spin) [24,25]. Until now, however, most studies have focused on the double FBs in the TBG because this twofold degeneracy originates from nondegenerate bands of the Dirac cones. An interesting and outstanding question is whether it is possible to realize FBs with higher degeneracy. Such an exploration is highly desirable as this realization will not only provide new insights into the origin of magic angles and FBs but also offer a more fruitful platform hosting diversified strongly correlated physics.

Beyond the twofold degeneracy of the moiré FBs, in this Letter, we show that an undiscovered generation of FBs with fourfold degeneracy emerges in the presence of spatially alternating magnetic fields, motivated by the electronic tunability in 2D systems with external uniform magnetic fields [26–29] modified by the hexagonal Haldane model [30]. Then, the Dirac cone of the monolayer acquires an additional magnetic phase φ. Importantly, this magnetic phase expands the solutions of magic angles to the complex eigenvalues of the Birman-Schwinger operator, in contrast to the real eigenvalues of the conventional TBG. Interestingly, some complex eigenvalues correspond to quadruple FBs (per valley/spin) with absolute flatness and nontrivial topology. Moreover, to reveal the origin of the quadruple bands, we show that the WFs can be generated by holomorphic functions with two real-space nodes, and the generating functions naturally lead to absolute flatness with the fourfold degeneracy. Finally, we discuss that the fourfold degeneracy can enrich correlated physics due to additional filling selections in these multifold FBs.

Model.—To be specific, we consider monolayer graphene with alternative magnetic fluxes in each triangle inside a hexagonal plaquette [Fig. 1(a)], similar to the Haldane model [30]. The blue (⊙) and yellow (⊗) triangles denote outward and inward to the plane fluxes, and the total flux through each hexagonal plaquette vanishes. With a Peierls substitution, the nearest-neighbor hopping acquires a magnetic phase φ. The Dirac Hamiltonian in the real space gains an additional phase and reads [31]

$$h_D^{\varphi}(\mathbf{r}) = -v_0 \begin{pmatrix} 0 & e^{-i\varphi} 2\partial \\ e^{i\varphi} 2\bar{\partial} & 0 \end{pmatrix}, \tag{1}$$

with $\bar{\partial} = (1/2i)(\partial_x + i\partial_y)$ and Fermi velocity v_0. The standard Dirac Hamiltonian is restored for monolayer graphene in the absence of magnetic flux. Then, we introduce a twist with angle θ between these two graphene layers [Fig. 1(b)]. We use the basis of $\Phi(\mathbf{r}) = (e^{i(\varphi/2)}\psi_A^t, e^{i(\varphi/2)}\psi_A^b, e^{-i(\varphi/2)}\chi_B^t, e^{-i(\varphi/2)}\chi_B^b)^\top$, which absorbs the magnetic phase, where t/b denotes the top/bottom graphene layers and A/B is the sublattice index. The chirally symmetric continuum model of TBG with alternating fluxes can be written as

$$H^{\varphi}(\mathbf{r}) = \begin{pmatrix} 0 & D^{\varphi *}(-\mathbf{r}) \\ D^{\varphi}(\mathbf{r}) & 0 \end{pmatrix}, \tag{2}$$

$$D^{\varphi}(\mathbf{r}) = \begin{pmatrix} 2\bar{\partial} & e^{i(\varphi+\beta)}\alpha_0 U(\mathbf{r}) \\ e^{i(\varphi-\beta)}\alpha_0 U(-\mathbf{r}) & 2\bar{\partial} \end{pmatrix}, \tag{3}$$

where $U(\mathbf{r}) = e^{-i\mathbf{q}_1\cdot\mathbf{r}} + e^{-i\mathbf{q}_2\cdot\mathbf{r}}e^{i\phi} + e^{-i\mathbf{q}_3\cdot\mathbf{r}}e^{-i\phi}$ with $\phi = 2\pi/3$. $\mathbf{q}_1 = k_\theta(-1, 0)$, $\mathbf{q}_{2,3} = k_\theta(1/2, \mp\sqrt{3}/2)$ are shown in Fig. 1(d) with $k_\theta = 2k_D \sin(\theta/2)$, and $k_D = |\mathbf{K}_{t/b}|$ is Dirac momentum in the monolayer graphene. The above Hamiltonian is characterized by a dimensionless real parameter $\alpha_0 e^{i\beta} = (\omega_{AB}/v_0 k_\theta)$, where ω_{AB} is the strength of the interlayer coupling with a constant phase β. Unlike the magnetic phase φ, the global phase β can be gauged away. For simplicity, we define a complex parameter $\alpha(\varphi) \equiv \alpha_0 e^{i\varphi}$. In addition, $H^{\varphi}(\mathbf{r})$ is off-diagonal as we consider the chiral limit, where we neglect intrasublattice (AA/BB) interlayer hopping. Since the twisted angle is small, we also neglect the rotation effect on the Dirac Hamiltonian $h_D^{\varphi}(\mathbf{r})$ [23]. In the momentum space, the interlayer coupling $U(\mathbf{r})$ can be illustrated by the network of the two Dirac cones with the extension of the momentum hoppings, where the hopping between the nearest-neighbor momentum sites acquires a phase $e^{i\varphi}$ owing to the alternative fluxes [Figs. 1(c) and 1(d)]. This nonzero phase plays a pivotal role in generating multifold FBs.

Multifold FBs.—We further discuss the conditions of absolutely zero-energy FBs for the above continuum model. After a gauge transformation $V = \mathrm{diag}(e^{-i\mathbf{k}\cdot\mathbf{r}}, e^{-i\mathbf{k}\cdot\mathbf{r}})$, the Hamiltonian $H_{\mathbf{k}}^{\varphi}(\mathbf{r}) = V^\dagger H^{\varphi}(\mathbf{r}) V$ can be written as

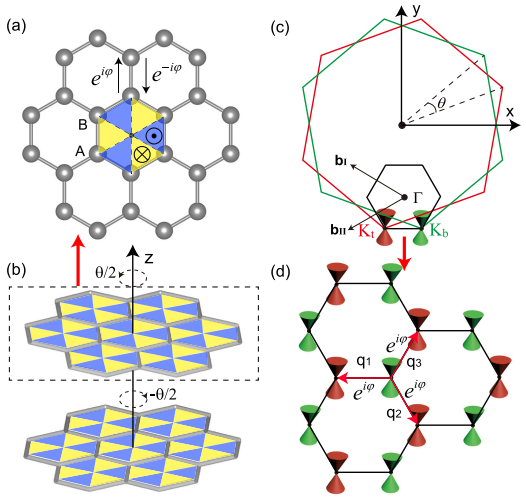

FIG. 1. (a) Distribution of periodic local magnetic fluxes in hexagonal plaquette of monolayer graphene with basis A and B. (b) TBG with alternative fluxes. (c) The two monolayer BZs with the twist form a moiré BZ. The red and green hexagons exhibit the BZs of the bottom and top layers, each rotated by an angle $\pm\theta/2$, and the black hexagon indicates the moiré BZ with momentum bases $\mathbf{b}_{\mathbf{I/II}} = \sqrt{3}k_\theta(-\sqrt{3}/2, \pm 1/2)$. (d) The reciprocal lattice structures. The interlayer coupling with the phase φ couple the red and green Dirac cones separately located in the top and bottom layers.

$$H_{\mathbf{k}}^{\varphi}(\mathbf{r}) = \begin{pmatrix} 0 & D_{\mathbf{k}}^{\varphi *}(-\mathbf{r}) \\ D_{\mathbf{k}}^{\varphi}(\mathbf{r}) & 0 \end{pmatrix}, \tag{4}$$

where $D_{\mathbf{k}}^{\varphi}(\mathbf{r}) \equiv D^{\varphi}(\mathbf{r}) - \mathbf{k}$ and the momentum $\mathbf{k}$ is defined in moiré BZ. The explicit form of $D_{\mathbf{k}}^{\varphi}(\mathbf{r})$ is given by

$$D_{\mathbf{k}}^{\varphi}(\mathbf{r}) = (2\bar{\partial} - \mathbf{k})(I + \alpha(\varphi)T_{\mathbf{k}}),$$
$$T_{\mathbf{k}} = (2\bar{\partial} - \mathbf{k})^{-1} \begin{pmatrix} 0 & U(\mathbf{r}) \\ U(-\mathbf{r}) & 0 \end{pmatrix}, \tag{5}$$

where $T_{\mathbf{k}}$ ($\mathbf{k} \neq 0$) is known as the Birman-Schwinger operator [24,25]. The appearance of zero-energy FBs implies that the determinant of Hamiltonian $H_{\mathbf{k}}^{\varphi}(\mathbf{r})$ vanishes for all $\mathbf{k}$, i.e., $\det(D_{\mathbf{k}}^{\varphi}(\mathbf{r})) = 0$. Because of $\det(2\bar{\partial} - \mathbf{k}) \neq 0$, for all nonzero $\mathbf{k}$ the matrix $[I - \alpha(\varphi)T_{\mathbf{k}}]$ should have at least one zero eigenvalue and for $\mathbf{k} = 0$ two low-energy states are fixed at zero energy. According to Refs. [24,25], the eigenvalues of $T_{\mathbf{k}}$ are independent of $\mathbf{k}$ and we can define a spectrum $\mathcal{A} = 1/\mathrm{Spec}(T_{\mathbf{k}})$ and a corresponding two-component eigenstate $\psi_{\mathbf{k}}^0(\mathbf{r})$. Therefore, once the parameter α is tuned to be one of the complex eigenvalues in $\mathcal{A}$, $D_{\mathbf{k}}^{\varphi}(\mathbf{r})\psi_{\mathbf{k}}^0(\mathbf{r}) = 0$ so that zero-energy FBs emerge in $H_{\mathbf{k}}^{\varphi}(\mathbf{r})$ and α has a magic value.

In the absence of the alternative magnetic field ($\varphi = 0$), the magic parameters α in the conventional TBG appear recursively on the real axis of spectrum $\mathcal{A}$ [24,25], and indicate the presence of double FBs [Fig. 2(a)]. When the

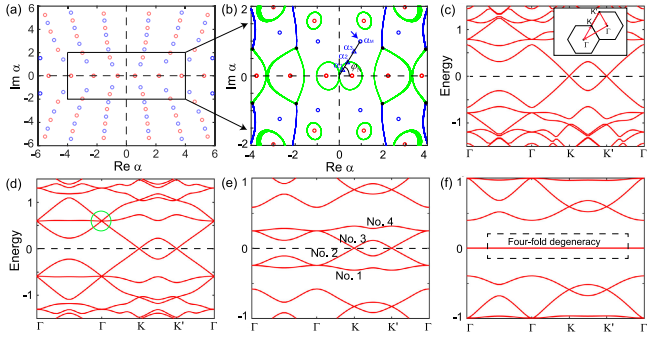

FIG. 2. (a) The spectra $\mathcal{A}$ shows the magic values of the dimensionless complex parameter α corresponding to double (red) and quadruple (blue) FBs. (b) The distribution of lowest energy band touching at the Γ point in the spectra $\mathcal{A}$. The band structures of the Hamiltonian $H^{\varphi}(\mathbf{r})$ with magnetic phase $\varphi_N = 0.254\pi$ in the different α_0 values marked by blue triangle in (b): (c) $\alpha_1 = 0.3e^{i\varphi_N}$, (d) $\alpha_2 = 0.55e^{i\varphi_N}$, (e) $\alpha_3 = 1.0e^{i\varphi_N}$, and (f) $\alpha_M = 1.379e^{i\varphi_N}$. The inset in (c) indicates the spectrum path in the moiré BZ. The green circle in (d) denotes band inversion between double degenerate and nondegenerate points at Γ.

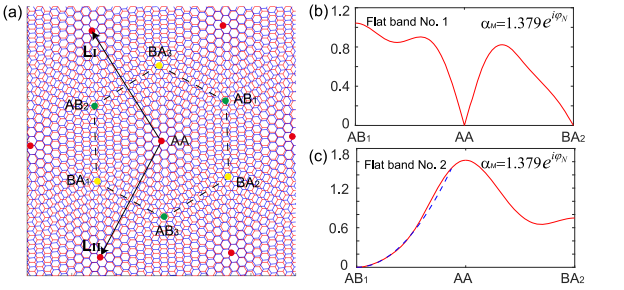

FIG. 3. (a) Schematic moiré pattern. The red, green, and yellow points indicate the **AA**, **AB**, and **BA** stacking points, and $\mathbf{L}_{\mathrm{I/II}} = 4\pi/3k_\theta(-1/2, \pm\sqrt{3}/2)$ are moiré lattice vector. (b) and (c) The norm of the two-component WFs $\psi_{\mathbf{K},1/2}(\mathbf{r})$ at the **K** point for FB No.1/2 at magic α_M. The blue dashed line in (c) represents the fitting of quadratic function.

alternative magnetic field is recovered, the magic values of α are expanded to the entire complex plane. The spectrum $\mathcal{A}$ exhibit no degeneracy (red circles) and twofold degeneracy (blue circles), respectively [Fig. 2(a)]. The nondegenerate and twofold degenerate eigenvalues correspond to double and quadruple FBs in magnetic TBG [31]. That is, the degeneracy of FBs is twice the degeneracy at magic values. Introducing the alternative fluxes extends magic parameters to more discrete values and leads to the emergence of quadruple FBs.

To investigate the evolution of the degeneracy in the spectra of the magnetic TBG, we take the complex eigenvalue closest to the origin in Fig. 2(b) as an example with magnetic phase $\varphi_N = 0.254\pi$ to demonstrate the changes of the low energy bands. The degeneracy of FBs is intimately related to the degeneracy of the lowest energy states at Γ in the TBG spectrum. To understand the transition of FBs with different degeneracies as α varies, we can track the band touch of the low-energy states at Γ [Fig. 2(b)]. The green (blue) curves represent a threefold (fourfold) band touching at Γ, resulting in band inversions between one singlet and one doublet (between two doublets). Importantly, the threefold degeneracy curves [Fig. 2(d)] separate the magic parameters α with double and quadruple FBs. Inside one of these degeneracy loops, two connected bands near zero energy in a direct gap [Fig. 2(c)] evolve to double FBs at magic α (red circles). As α crosses a threefold degeneracy line, the band inversion changes two connected bands to four connected ones in the gap [Fig. 2(e)]. Outside these degeneracy loops, the four connected bands evolve to quadruple FBs [Fig. 2(f)] at magic α (blue circles). Then, as discussed in the Supplemental Material [31], we consider the effect of intrasublattice interlayer coupling, which can result in a slight dispersion of the quadruple FBs. In addition, within the quadruple FBs, two of them (No. 2/3) that constitute Dirac points possess Chern numbers of ± 1 while the Chern numbers of the remaining two bands (No. 1/4) vanish.

Origin of quadruple FBs.—In the conventional TBG, the key to rigorously showing the emergence of the double absolutely FBs is that at the magic angles, the absolute values of the WFs with the zero energy at $\mathbf{K}/\mathbf{K}'$ have a linear-momentum-dispersion node at BA/AB stacking [Fig. 3(a)]. Using this WF at **K**, one generates two eigenfunctions with zero energy at any momentum point [23]. For the magnetic TBG, we can use a similar approach to show the absolute flatness of the quadruple bands at magic α by identifying the nodes of the WFs at **K** and extending this function to the entire Moiré BZ.

To distinguish the quadruple FBs, consider α slightly away from the magic value [Fig. 2(e)]. The two lowest bands are labeled by No.1/2, and the remaining two bands can be generated by chiral symmetry operator $S = \tau_z\sigma_0$. In addition, due to C_2T symmetry, the nondegenerate four-component WF $\Psi_{\mathbf{k},i}(\mathbf{r})$ can be expressed by a two-component vector $\psi_{\mathbf{k},i}(\mathbf{r})$ with band index $i = 1, 2$. At the magic $\alpha_M = 1.379e^{i\varphi_N}$, the norm $[\psi^{\dagger}_{\mathbf{K},1/2}(\mathbf{r})\psi_{\mathbf{K},1/2}(\mathbf{r})]^{1/2}$ shows that for FB No.1 at **K**, two nodes appear at the AA and BA stacking with a dominant linear real-space dependence [Fig. 3(b)]. Meanwhile, for FB No.2 at **K**, there is only one node at the AB stacking, and the norm exhibits real-space quadratic dependence near it, implying a second order node [Fig. 3(c)]. These nodal features in sharp contrast to the conventional TBG are the important ingredients for the absolute flatness of the quadruple bands.

To simplify the absolute flatness problem, we focus on the solution of $D^{\varphi}(\mathbf{r})\psi_{\mathbf{k}}(\mathbf{r}) = 0$ for all $\mathbf{k}$. Previously, we numerically obtain the two-component WFs $\psi_{\mathbf{K}}(\mathbf{r})$ pinned at zero energy at **K**, which is a good starting point to construct WFs of the FBs at other $\mathbf{k}$. As $\mathbf{k} \neq \mathbf{K}$, the conjectural WF can be written as $\psi_{\mathbf{k}}(\mathbf{r}) \equiv f_{\mathbf{k}}(z)\psi_{\mathbf{K}}(\mathbf{r})$ with

$z = x + iy$ since $D^{\varphi}(\mathbf{r})\psi_{\mathbf{k}}(\mathbf{k}) = f_{\mathbf{k}}(z)[D^{\varphi}(\mathbf{r})\psi_{\mathbf{K}}(\mathbf{r})] = 0$. The holomorphic function $f_{\mathbf{k}}(z)$ is either a constant or unbounded by Liouville's theorem, indicating that $f_{\mathbf{k}}(z)$ is meromorphic and thus has poles as $\mathbf{k} \neq \mathbf{K}$. The eigenfunctions $\psi_{\mathbf{k}}(\mathbf{r})$ are valid when the poles of $f_{\mathbf{k}}(z)$ are smoothed out by the nodes of $\psi_{\mathbf{K}}(\mathbf{r})$ in the Moiré unit cell. For the double FBs in the conventional TBG, only one node appears in $\psi_{\mathbf{K}}(\mathbf{r})$. Differently, for the quadruple FBs, a second-order node at the AB stacking point emerges in $\psi_{\mathbf{K},2}(\mathbf{r})$ of the band No. 2 at the magic α, while there are already two linear nodes in the $\psi_{\mathbf{K},1}(\mathbf{r})$ of the band No.1. We note that $\psi_{\mathbf{K},2}(\mathbf{r})$ is always pinned at the zero-energy and possesses the node only at the magic α. In contrast, $\psi_{\mathbf{K},1}(\mathbf{r})$ always has the two nodes and drops to zero energy at the magic α. The zero energy and the presence of the nodes at the magic α lead to the solution of the zero-energy absolutely FBs in the entire Moiré BZ.

We turn to the construction of WFs for the quadruple FBs. To cancel the poles of $\Psi_{\mathbf{K}}(\mathbf{r})$, we choose two theta functions in the denominator of $f_{\mathbf{k}}(z)$ and adjust $f_{\mathbf{k}}(z)$ to render the two-component WF $\psi_{\mathbf{k}}(\mathbf{r})$ to obey the Bloch boundary conditions on moiré lattice vectors $\mathbf{L}_{\mathrm{I/II}}$, namely, $\psi_{\mathbf{k}}(\mathbf{r} + \mathbf{L}_{\mathrm{I/II}}) = e^{i\mathbf{k}\cdot\mathbf{L}_{\mathrm{I/II}}} U \psi_{\mathbf{k}}(\mathbf{r})$ with $U = \mathrm{diag}(e^{-i\phi}, e^{i\phi})$ [23]. The analytical expressions for the quadruple FB WFs $\Psi_{\mathbf{k},1/2}(\mathbf{r})$ read

$$\Psi_{\mathbf{k},1}(\mathbf{r}) = \frac{\vartheta_{a_1,b_1}(\nu|\omega)\vartheta_{a_1',b_1'}(\nu|\omega)}{\vartheta_{\frac{1}{2},\frac{1}{2}}(\nu|\omega)\vartheta_{\frac{5}{6},\frac{7}{6}}(\nu|\omega)}\Psi_{\mathbf{K},1}(\mathbf{r}), \tag{6}$$

$$\Psi_{\mathbf{k},2}(\mathbf{r}) = \frac{\vartheta_{a_2,b_2}(\nu|\omega)\vartheta_{a_2',b_2'}(\nu|\omega)}{[\vartheta_{\frac{7}{6},\frac{5}{6}}(\nu|\omega)]^2}\Psi_{\mathbf{K},2}(\mathbf{r}), \tag{7}$$

with $\nu = z/L_{\mathrm{I}}$, $\omega = (L_{\mathrm{II}}/L_{\mathrm{I}}) = e^{i\phi}$ and $L_{\mathrm{I/II}} = (\mathbf{L}_{\mathrm{I/II}})_x + i(\mathbf{L}_{\mathrm{I/II}})_y$. To satisfy the Bloch boundary conditions, the rational characteristics a and b obey

$$a_i + a_i' = \frac{1}{3} + \frac{(\mathbf{k}-\mathbf{K})\cdot\mathbf{L}_{\mathrm{I}}}{2\pi} + n_{\mathrm{I}}, \tag{8}$$

$$b_i + b_i' = \frac{2}{3} - \frac{(\mathbf{k}-\mathbf{K})\cdot\mathbf{L}_{\mathrm{II}}}{2\pi} + n_{\mathrm{II}}, \tag{9}$$

where n_{I} and n_{II} are arbitrary integers due to the lattice transnational symmetry. The definition of the theta function $\vartheta_{a,b}(\nu|\omega)$ and the detailed derivations of Eqs. (6) and (7) are provided in the Supplemental Material [31]. The equations above cannot determine the explicit expressions of the rational characteristics, which are functions of $\mathbf{k}$, unless the node locations are given.

To prove the absolutely FBs, we numerically calculate the flat-band WFs from Hamiltonian $H^{\varphi}(\mathbf{r})$ and determine the node locations. The node locations fix the values of a, b in theta functions Eqs. (6) and (7). To confirm the validity of the WF expressions in Eqs. (6) and (7), we first select a general point $\mathbf{P}$ as an example. Figures 4(a) and 4(b) show the norm of WFs $\psi_{\mathbf{k},1/2}$ for FB No.1/2 at $\mathbf{k} = \mathbf{P}$, where the WFs from Hamiltonian $H^{\varphi}(\mathbf{r})$ and Eqs. (6) and (7) are labeled in red squares and blue triangles, respectively. We find a good agreement between them, and the agreement can be extended to other general $\mathbf{k}$ points [31]. Therefore, through the evolution of nodes and real-space WF, we have verified the validity of WF in Eqs. (6) and (7), and quadruple FBs are absolutely flat. In Supplemental Material [31], we further confirm the validity of the relation between Eqs. (8) and (9) and nodal coordinates.

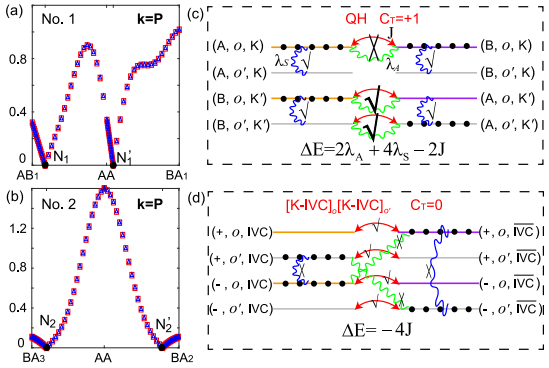

FIG. 4. (a) and (b) The norm of WFs $\psi_{\mathbf{k},1/2}(\mathbf{r})$ for FBs No.1/2 at $\mathbf{k} = \mathbf{P}$ with $\mathbf{P} = 0.5\mathbf{b_I} - 0.3\mathbf{b_{II}}$. $N_{1/2}$ and $N'_{1/2}$ are corresponding nodal points. (c) and (d) The configurations for QH and $[\mathrm{K\text{-}IVC}]_o[\mathrm{K\text{-}IVC}]_{o'}$ states with $C_T = +1$ and $C_T = 0$, and the IVC bases are a coherent superposition of two valley FB bases and the relations can be found in Supplemental Material [31]. The FBs labeled by gray, orange, and pink lines possess Chern number $C = 0$, $C = +1$, and $C = -1$. The symbols $\surd$ or $\times$ indicate whether the processes are permitted or forbidden.

Correlation states.—The presence of multiplefold FBs provides an excellent platform for exploring correlated quantum states. Besides the valley and sublattice degrees of freedom in double FBs [39], the quadruple FBs introduce an emergent orbital degree of freedom, which can significantly enrich the correlated states. Within the quadruple FBs, two of them (No. 2/3) that constitute Dirac points possess exhibit Chern numbers of ± 1 labeled by the o orbital while the Chern numbers of the remaining two bands (No. 1/4 o' orbital) vanish. Therefore, in the spinless case with the two valleys, the total Chern numbers of ± 2 can be realized in the quantum Hall (QH) states at integer filling [39–41]. With a fractional filling of the high-Chern-number FBs [42], fractional quantum Hall states at a variety of filling factors can be realized. We use the half-filling scenario (four out of the eight FBs are filled) as a primary example. Assuming the intrasublattice-intraorbital interaction scale is much larger than other scales, the ground state of this interaction is the one where each of the eight bands is completely filled or empty [39]. There are $C_4^8 = 70$ degenerate many-body ground states [31], while only $C_2^4 = 6$ ground states are present in the conventional TBG.

However, for intervalley-coherent (IVC) states, the types of ground states increase significantly, and an exotic combination of the QH and IVC states, such as time-reversal IVC (T-IVC) and Kramers IVC (K-IVC) states, can be realized [31,39]. We schematically show the two representative examples: orbital related QH and $[\text{K-IVC}]_o[\text{K-IVC}]_{o'}$ states in Figs. 4(c) and 4(d). The former state features three fully occupied o-orbital FBs and one fully occupied o'-orbital FB, where the o orbital can contribute to the Chern number $C_T = +1$. In the latter state, both o- and o'-orbital sectors feature K-IVC states with antiparallel pseudospin between two orbitals.

Now we introduce the effect of single-particle dispersion, intersublattice–intraorbital interaction and intrasublattice–interorbital interaction as perturbations, so the high degeneracy of the ground states can be lifted. The single-particle dispersion introduces a hopping between the horizontal pair states (A $\leftrightarrow$ B) [denoted by red curves in Fig. 4(c)], yielding a energy reduction of the order of J. For the latter two interaction terms, the corresponding energy increments are proportional to $\lambda_{A/S}\sum_{i=1,2}\hat{n}_i(1-\hat{n}_{\bar{i}})$, where $\hat{n}_i$ is the particle number operator for one of the horizontal (A $\leftrightarrow$ B) or vertical ($o \leftrightarrow o'$) pair states. They are denoted by green and blue wavy lines in Figs. 4(c) and 4(d), respectively. It is evident that three types of energy corrections are nonzero when only one of the pair states is occupied. Therefore, the energy correction can be formulated as $\Delta E = N_A\lambda_A + N_S\lambda_S - N_J J$ [43]. From the energy, we identify the anti-orbital K-IVC state in Fig. 4(d) as the ground state at charge neutrality. Varying doping and twisted angles may induce transitions between different correlated states, necessitating detailed Hartree Frock calculations, which we defer to future investigations.

Discussion and conclusion.—In recent experiments, FBs have been achieved in twisted-bilayer optical lattice systems [44]. Moreover, the experimental achievement of alternative magnetic flux has been demonstrated in triangular and honeycomb optical lattices [45,46]. These developments clearly indicate that the experimental realization of our proposed model is both feasible and highly promising in optical lattice. In summary, introducing alternative fluxes opens a venue for undiscovered multiple magic angles and another generation of absolutely FBs with higher degeneracy. Specifically, we report that the double and quadruple FBs appear recursively in TBG with alternative magnetic fluxes, and adjusting the twisted angle and magnetic phase can control the transition between double and quadruple FBs. The quadruple FBs share the same origin with the conventional TBG, and by using holomorphic functions, we can generate analytical WFs to show the absolute flatness of the quadruple bands. Moreover, additional orbitals in the quadruple bands lead to more diversified strongly correlated physics. Our Letter demonstrates that the magnetic phase is a unique tuning parameter to tailor the electronic structure in moiré twistronics, which can significantly enrich topological and correlated phenomena.

We thank Zhida Song, Simon Becker, and Xu Zhang for the helpful discussions and comments. C.-K. C. was supported by Japan Science and Technology Agency (JST) as part of Adopting Sustainable Partnerships for Innovative Research Ecosystem, Grant No. JPMJAP2318, and by JST Presto Grant No. JPMJPR2357. X. X. W. is supported by the National Key R&D Program of China (Grant No. 2023YFA1407300) and the National Natural Science Foundation of China (Grant No. 12047503).

*xxwu@itp.ac.cn
†ching-kai.chiu@riken.jp

[1] R. Bistritzer and A. H. MacDonald, Proc. Natl. Acad. Sci. U.S.A. **108**, 12233 (2011).
[2] Y. Cao, V. Fatemi, A. Demir, S. Fang, S. L. Tomarken, J. Y. Luo, J. D. Sanchez-Yamagishi, K. Watanabe, T. Taniguchi, E. Kaxiras, R. C. Ashoori, and P. Jarillo-Herrero, Nature (London) **556**, 80 (2018).
[3] Y. Cao, V. Fatemi, S. Fang, K. Watanabe, T. Taniguchi, E. Kaxiras, and P. Jarillo-Herrero, Nature (London) **556**, 43 (2018).
[4] H. C. Po, L. Zou, A. Vishwanath, and T. Senthil, Phys. Rev. X **8**, 031089 (2018).
[5] X. Lu, P. Stepanov, W. Yang, M. Xie, M. A. Aamir, I. Das, C. Urgell, K. Watanabe, T. Taniguchi, G. Zhang, A. Bachtold, A. H. MacDonald, and D. K. Efetov, Nature (London) **574**, 653 (2019).
[6] G. Chen, L. Jiang, S. Wu, B. Lyu, H. Li, B. L. Chittari, K. Watanabe, T. Taniguchi, Z. Shi, J. Jung, Z. Yuanbo, and W. Feng, Nat. Phys. **15**, 237 (2019).
[7] G. Chen, A. L. Sharpe, P. Gallagher, I. T. Rosen, E. J. Fox, L. Jiang, B. Lyu, H. Li, K. Watanabe, T. Taniguchi, J. Jung, Z. Shi, D. Goldhaber-Gordon, Y. Zhang, and F. Wang, Nature (London) **572**, 215 (2019).
[8] T. Devakul, V. Crépel, Y. Zhang, and L. Fu, Nat. Commun. **12**, 6730 (2021).
[9] A. Ghiotto, E.-M. Shih, G. S. Pereira, D. A. Rhodes, B. Kim, J. Zang, A. J. Millis, K. Watanabe, T. Taniguchi, J. C. Hone, L. Wang, C. R. Dean, and A. N. Pasupathy, Nature (London) **597**, 345 (2021).
[10] P. J. Ledwith, A. Vishwanath, and E. Khalaf, Phys. Rev. Lett. **128**, 176404 (2022).
[11] C. Shen, Y. Chu, Q. Wu, N. Li, S. Wang, Y. Zhao, J. Tang, J. Liu, J. Tian, K. Watanabe, T. Taniguchi, R. Yang, Z. Y. Meng, D. Shi, O. V. Yazyev, and G. Zhang, Nat. Phys. **16**, 520 (2020).
[12] U. Zondiner, A. Rozen, D. Rodan-Legrain, Y. Cao, R. Queiroz, T. Taniguchi, K. Watanabe, Y. Oreg, F. von Oppen, A. Stern, E. Berg, P. Jarillo-Herrero, and S. Ilani, Nature (London) **582**, 203 (2020).
[13] D. Mumford, *Tata Lectures on Theta I, Progress in Mathematics* (1983), Vol. 28, pp. XIII, 240.
[14] I. Das, C. Shen, A. Jaoui, J. Herzog-Arbeitman, A. Chew, C.-W. Cho, K. Watanabe, T. Taniguchi, B. A. Piot,

B. A. Bernevig, and D. K. Efetov, Phys. Rev. Lett. **128**, 217701 (2022).
[15] M. Christos, S. Sachdev, and M. S. Scheurer, Phys. Rev. X **12**, 021018 (2022).
[16] J. M. Park, Y. Cao, K. Watanabe, T. Taniguchi, and P. Jarillo-Herrero, Nature (London) **590**, 249 (2021).
[17] M. Yankowitz, S. Chen, H. Polshyn, Y. Zhang, K. Watanabe, T. Taniguchi, D. Graf, A. F. Young, and C. R. Dean, Science **363**, 1059 (2019).
[18] P. Stepanov, I. Das, X. Lu, A. Fahimniya, K. Watanabe, T. Taniguchi, F. H. Koppens, J. Lischner, L. Levitov, and D. K. Efetov, Nature (London) **583**, 375 (2020).
[19] M. Serlin, C. L. Tschirhart, H. Polshyn, Y. Zhang, J. Zhu, K. Watanabe, T. Taniguchi, L. Balents, and A. F. Young, Science **367**, 900 (2020).
[20] A. L. Sharpe, E. J. Fox, A. W. Barnard, J. Finney, K. Watanabe, T. Taniguchi, M. A. Kastner, and D. Goldhaber-Gordon, Science **365**, 605 (2019).
[21] W.-Y. He, D. Goldhaber-Gordon, and K. T. Law, Nat. Commun. **11**, 1650 (2020).
[22] C.-C. Tseng, X. Ma, Z. Liu, K. Watanabe, T. Taniguchi, J.-H. Chu, and M. Yankowitz, Nat. Phys. **18**, 1038 (2022).
[23] G. Tarnopolsky, A. J. Kruchkov, and A. Vishwanath, Phys. Rev. Lett. **122**, 106405 (2019).
[24] S. Becker, M. Embree, J. Wittsten, and M. Zworski, Phys. Rev. B **103**, 165113 (2021).
[25] S. Becker, M. Embree, J. Wittsten, and M. Zworski, Probab. Math. Phys. **3**, 69 (2022).
[26] V. o. T. Phong and E. J. Mele, Phys. Rev. Lett. **128**, 176406 (2022).
[27] J. Dong, J. Wang, and L. Fu, arXiv:2208.10516.
[28] J. Herzog-Arbeitman, A. Chew, and B. A. Bernevig, Phys. Rev. B **106**, 085140 (2022).
[29] Y. Guan, O. V. Yazyev, and A. Kruchkov, Phys. Rev. B **106**, L121115 (2022).
[30] F. D. M. Haldane, Phys. Rev. Lett. **61**, 2015 (1988).
[31] See Supplemental Material at http://link.aps.org/supplemental/10.1103/PhysRevLett.132.246401, which includes Refs. [32–38], for comprehensive derivations and discussions on flat band wave functions, correlation states, and others.
[32] Z.-D. Song, B. Lian, N. Regnault, and B. A. Bernevig, Phys. Rev. B **103**, 205412 (2021).
[33] D. Mumford, Prog. Math. **28**, 240 (1983).
[34] B. A. Bernevig, Z.-D. Song, N. Regnault, and B. Lian, Phys. Rev. B **103**, 205413 (2021).
[35] P. J. Ledwith, E. Khalaf, and A. Vishwanath, Ann. Phys. (Amsterdam) **435**, 168646 (2021), special issue on Philip W. Anderson.
[36] N. R. Cooper, J. Dalibard, and I. B. Spielman, Rev. Mod. Phys. **91**, 015005 (2019).
[37] L. Tarruell, D. Greif, T. Uehlinger, G. Jotzu, and T. Esslinger, Nature (London) **483**, 302 (2012).
[38] X.-W. Luo and C. Zhang, Phys. Rev. Lett. **126**, 103201 (2021).
[39] N. Bultinck, E. Khalaf, S. Liu, S. Chatterjee, A. Vishwanath, and M. P. Zaletel, Phys. Rev. X **10**, 031034 (2020).
[40] Y.-H. Zhang, D. Mao, Y. Cao, P. Jarillo-Herrero, and T. Senthil, Phys. Rev. B **99**, 075127 (2019).
[41] Y.-H. Zhang, D. Mao, and T. Senthil, Phys. Rev. Res. **1**, 033126 (2019).
[42] P. J. Ledwith, G. Tarnopolsky, E. Khalaf, and A. Vishwanath, Phys. Rev. Res. **2**, 023237 (2020).
[43] The parameters $N_{A/S/J}$ are determined by the number of active interacting and hopping channels between pair states and $\lambda_{A/S}, J > 0$.
[44] Z. Meng, L. Wang, W. Han, F. Liu, K. Wen, C. Gao, P. Wang, C. Chin, and J. Zhang, Nature (London) **615**, 231 (2023).
[45] J. Struck, M. Weinberg, C. Ölschläger, P. Windpassinger, J. Simonet, K. Sengstock, R. Höppner, P. Hauke, A. Eckardt, M. Lewenstein, and L. Mathey, Nat. Phys. **9**, 738 (2013).
[46] G. Jotzu, M. Messer, R. Desbuquois, M. Lebrat, T. Uehlinger, D. Greif, and T. Esslinger, Nature (London) **515**, 237 (2014).